Journal of Materials Chemistry A

ROYAL SOCIETY OF CHEMISTRY

PAPER

View Article Online
View Journal | View Issue

Check for updates

Cite this: J. Mater. Chem. A, 2023, 11, 15739

Low thermal conductivity in $Bi_8CsO_8SeX_7$ (X = Cl, Br) by combining different structural motifs†

Jon A. Newnham, Quinn D. Gibson, ‡ T. Wesley. Surta, Alexandra Morscher, Troy D. Manning, Luke M. Daniels, John B. Claridge and Matthew J. Rosseinsky *

Received 17th March 2023
Accepted 30th June 2023

DOI: 10.1039/d3ta01630g

rsc.li/materials-a

Understanding the structure–property relationships of materials in order to supress thermal conductivity is crucial for developing efficient thermoelectric generators and thermal barrier coatings. Low thermal conductivity materials can often contain a single dominant phonon scattering mechanism. Here, we highlight how combining different structural features into one material can aid in the design and identification of new materials with low thermal conductivities. We synthesise two new mixed-anion materials, $Bi_8CsO_8SeX_7$ (X = Cl and Br), with low thermal conductivities of 0.27(2) and 0.22(2) W m^{-1} K^{-1} respectively, measured along their *c*-axes at room temperature. The $Bi_8CsO_8SeX_7$ materials possess a combination of bond strength hierarchies, Cs^+ vacancies, and low frequency Cs^+ rattling. These different features significantly inhibit phonon transport along different crystallographic directions. Due to sharp bond strength contrast between the van der Waals gaps and $[Bi_2O_2]^{2+}$ layers, the $Bi_8CsO_8SeX_7$ materials exhibit thermal conductivities <50% of the theoretical minimum when measured along the stacking direction. Conversely, the thermal conductivity associated with the *ab*-plane is reduced by Cs^+ rattling when compared to the structurally and compositionally related BiOCl.

Open Access Article. Published on 30 June 2023. Downloaded on 12/7/2025 10:16:05 AM.
This article is licensed under a Creative Commons Attribution 3.0 Unported Licence.

1. Introduction

Materials that possess low thermal conductivities are of note as they are important for many applications including thermal barrier coatings and as thermoelectric generators and coolers.[1–3] These materials are also of interest in probing the fundamental lower limitations of thermal conductivity in the solid state.[4–7] Mechanisms to scatter phonons and reduce thermal conductivity can be introduced at a range of length scales including alloying, nanostructuring, and at grain boundaries.[8–10] However, these strategies often have the adverse effect of simultaneously reducing the electrical mobilities of such materials.[11] As such, it is desirable to synthesise materials with low thermal conductivities that are intrinsic to the phonon band structure.[12]

Understanding the mechanisms that determine thermal transport in these materials allows us to design and identify new materials with intrinsically low thermal conductivities based on their structure.[13,14] These materials often have structural features in common such as bond strength contrast, heavy elements, rattling ions, "liquid-like" movement of ions, and s^2 lone pairs.[14–20]

Combining these strategies to minimise thermal conductivity can be achieved by introducing different structural motifs through the discovery of new materials. For example, $Bi_4O_4SeCl_2$ is a superlattice of BiOCl and Bi_2O_2Se, and exhibits thermal transport properties similar to BiOCl along its *c*-axis, and to Bi_2O_2Se along its *ab*-plane.[14] The resulting material has an extremely low and highly anisotropic thermal conductivity, highlighting the effectiveness of combining different structural motifs into one material. Mixed anion materials such as Bi_2O_2Se and BiOCl often display a range of interesting properties including high catalytic activities, high anionic conductivities, and also low thermal conductivities.[21–23] This is due to the structural and compositional diversity provided by the use of multiple anions, and the resulting tunability of the materials' properties.[24]

Despite a range of structural features that can reduce the thermal conductivity of a material, it cannot be arbitrarily low. The amorphous limit describes the minimum thermal

Department of Chemistry, University of Liverpool, Crown Street, Liverpool, L69 7ZD, UK. E-mail: m.j.rosseinsky@liverpool.ac.uk

† Electronic supplementary information (ESI) available: Rietveld fits of neutron diffraction patterns for $Bi_8CsO_8SeX_7$, PXRD patterns of the additional materials discussed and their extracted lattice parameters, results of thermal and water stability experiments, plots from the DC polarisation measurements at different voltages, and detailed descriptions of the heat capacity and thermal conductivity models can be found in the ESI. The crystal structures of $Bi_8CsO_8SeCl_7$ and $Bi_8CsO_8SeBr_7$ are described in the respective crystallographic information files deposited with CSD accession codes 2246936-2246945. The underlying data generated in this study can be found at https://doi.org/10.17638/datacat.liverpool.ac.uk/2156. See DOI: https://doi.org/10.1039/d3ta01630g

‡ Q. D. Gibson is now based at: Department of Chemistry, University of Aberdeen, Aberdeen AB24 3UE, United Kingdom.

Open Access Article. Published on 30 June 2023. Downloaded on 12/7/2025 10:16:05 AM.
This article is licensed under a Creative Commons Attribution 3.0 Unported Licence.

conductivity (κ_{min}) of a crystalline material based on two assumptions: (1) the phonon velocities in a material are equal to the Debye velocities, and (2) there is negligible difference between the acoustic and optical phonon velocities.[7]

BiOCl, Bi_2O_2Se, and $Bi_4O_4SeCl_2$ are mixed-anion materials with related structures, compositions, and low thermal conductivities.[14] Here, we introduce two new mixed-anion materials into this family, $Bi_8CsO_8SeX_7$ (X = Cl and Br), and find that they have low thermal conductivities of 0.27(2) and 0.22(2) W m^{-1} K^{-1} respectively at room temperature along their stacking (c) axes. These are lower than the theoretical minimum due to a breakdown of the underlying assumptions used to calculate the amorphous limit. Herein, we show that the low thermal conductivities originate from a combination of different structural features including sharp bond strength contrast, Cs^+ vacancies, and low frequency Cs^+ rattling that interfere with phonon transport.

2. Methods

2.1. Synthesis

Powders of Bi_2O_3 (99.999%), BiOCl (99.999%), CsCl (99.999%), $BiBr_3$ (99.999%), and CsBr (99.999%), as well as Bi_2Se_3 pieces (99.999%) were purchased from Alfa Aesar. The Bi_2Se_3 pieces were hand ground into a powder using a pestle and mortar before use.

$Bi_8CsO_8SeCl_7$ was identified as a target material through simultaneous Bi^{3+}-for-Pb^{2+} and Se^{2-}-for-Cl^- substitutions in $Pb_{0.6}Bi_{3.4}Cs_{0.6}O_4Cl_4$.[25] Bulk samples of $Bi_8CsO_8SeCl_7$ were synthesized by hand grinding powders of BiOCl, Bi_2O_3, Bi_2Se_3, and CsCl in stoichiometric amounts in an agate pestle and mortar. The resulting mixture was sealed in a 6 mm radius quartz ampule that was evacuated to 10^{-4} mbar and fired at 700 °C for 12 h using heating and cooling rates of 5 °C min^{-1}. $Bi_8CsO_8SeBr_7$ was synthesised by grinding $BiBr_3$, Bi_2O_3, Bi_2Se_3, and CsBr in stoichiometric amounts in an Ar-filled glovebox (O_2 < 0.5 ppm, H_2O < 0.5 ppm), and firing them in an evacuated quartz ampule using the same conditions as used to make the chloride. A total of 3 g of each material was synthesised for physical property measurements, and a further 5 g was synthesised for neutron diffraction measurements. We were unable to synthesise the iodide as a pure phase under similar conditions.

2.2. Processing

Pure powders of each material (~1.0 g) were pressed into dense pellets (≈95% theoretical density) by spark plasma sintering using a commercial Thermal Technology LLC DCS10 furnace. The pressure and temperature were set to 800 MPa and 400 °C, and was dwelled for 5 min in a 10^{-3} mbar vacuum. The heating and pressure ramp rates were set to 50 °C min^{-1} and 100 MPa min^{-1}, respectively. The pellets were pressed in a 10 mm diameter Co-bonded tungsten carbide die that was lined with graphite foil. After pressing, pellets were removed from the die and any excess graphite foil was polished from the surface of the pellet using SiC paper.

2.3. Neutron powder diffraction

Time-of-flight (TOF) neutron powder diffraction data were collected with a d-spacing range of ~0.2–6 Å on samples contained in vanadium cans using the Nanoscale-Ordered Materials Diffractometer (NOMAD, beamline 1B) at the Spallation Neutron Source (SNS), Oak Ridge National Laboratory. Rietveld refinements of the neutron diffraction data were modelled using TOPAS Academic V5.[26] The TOF x-axis was calibrated using a high purity silicon standard, and the lattice parameters of each material were refined using the highest resolution data set (Bank 5), and then fixed. Across banks 1–5, the background was refined using a Chebyshev function with eight terms and a March–Dollase parameter was added to account for the preferred packing orientation of the powder within the vanadium cans.

The structures of $Bi_8CsO_8SeX_7$ (X = Cl and Br) were determined using the structure of $Bi_{3.4}Pb_{0.6}Cs_{0.6}O_4Cl_4$ as a starting model and refining the atomic positions, displacement parameters, and occupancies of the appropriate sites against neutron diffraction data from banks 1–5 of NOMAD simultaneously.[25]

2.4. Variable temperature powder X-ray diffraction

Synchrotron variable temperature powder X-ray diffraction (VT-PXRD) data were collected at Diamond Light Source at beamline I11 using a wavelength of $\lambda = 0.825379$ Å. Data were collected at angles of 2°–75° 2θ using a position sensitive detector from 100–500 K, in 50 K steps. The sample was diluted with amorphous SiO_2 and loaded into a 0.3 mm diameter borosilicate glass capillary.

The structure of $Bi_8CsO_8SeCl_7$ that was obtained from the neutron powder diffraction measurements was used as the starting model for the refinements of the VT-PXRD data. Only the background, lattice parameters, atomic positions, and atomic displacement parameters were refined against the data at each temperature. The background was modelled using a Chebyshev polynomial function with twelve parameters. A small, broad background peak at ~12° 2θ originates from the amorphous SiO_2 used to dilute the sample and was fit using a single broad pseudo-Voigt peak that was summed with the background function.

The Einstein and Debye temperatures associated with a particular site can be extracted using the gradient of $U_{iso}(T)$ using eqn (1) and (2), respectively.[27]

$$U_{iso} = \hbar^2 T/(mk_B\theta_E{}^2 4\pi^2) \quad (1)$$

$$U_{iso} = 3\hbar^2 T/(mk_B\theta_D{}^2 4\pi^2) \quad (2)$$

Here, $\hbar$ is the Planck constant, T is the temperature, m is the mass of the associated atom, k_B is Boltzmann constant. θ_E and θ_D are the Einstein and Debye temperatures, respectively.

2.5. Heat capacity and thermal conductivity

Heat capacities were measured in the temperature range of 2–300 K on a small piece of a densified pellet (<15 mg) using the

 This journal is © The Royal Society of Chemistry 2023

Open Access Article. Published on 30 June 2023. Downloaded on 12/7/2025 10:16:05 AM.
This article is licensed under a Creative Commons Attribution 3.0 Unported Licence.

heat capacity option on the Quantum Design Physical Properties Measurement System (PPMS) using the relaxation method. The piece was mounted to the sample puck using N-grease, and the contribution from the puck and grease was measured and subtracted from the final result to obtain the heat capacity of the material.

The thermal conductivities of $Bi_8CsO_8SeX_7$ (X = Cl and Br) pellets were measured both parallel and perpendicular to the pressing direction using a Quantum Design Physical Properties Measurement System using the thermal transport option in the temperature range of 2–300 K. Parallel measurements were made using a two-contact method, while perpendicular measurements were made using a four-contact method on a bar cut out of the pellet using a low-speed saw and diamond cutting blade.

Above room temperature, the thermal conductivities were measured by the laser flash method using a Netzsch LFA 457. Measurements were made under dynamic vacuum with a heating rate of 3 K min^{-1} with 5 min equilibration at each temperature. Thermal diffusivities were obtained by fitting the Cowan model to raw data. The thermal conductivities were then obtained by multiplying the thermal diffusivity, sample density, and heat capacity (assumed to be 3R at high temperatures).

Heat capacity data were modelled using a linear combination of Debye and Einstein terms, and the in-plane thermal conductivities were modelled using the Debye–Callaway model. Full details of modelling the heat capacity and thermal conductivity are given in the ESI,† along with the extracted parameters.

2.6. Alternating current (AC) impedance spectroscopy and direct current (DC) polarization

A dense pellet of $Bi_8CsO_8SeCl_7$ was transferred to an Ar glovebox and sputtered with a 300 nm thickness Au coating using a Quorum Q150R sputter coater. Any gold that had sputtered onto the side of the pellets was removed by light polishing with SiC paper. AC impedance measurements were performed in the same glovebox at room temperature using a Keysight E4990A impedance analyser over a frequency range of 2 MHz to 20 Hz (with an amplitude of 100 mV). The same pellet was used for room temperature DC potentiation polarization measurements by applying constant potentials of 0.05, 0.1, 0.3, and 0.5 V for 7000 s and monitoring the current variation with time.

3. Results and discussion

3.1. Structure and composition

Rietveld fits against NOMAD neutron powder diffraction data (Fig. 1a and b, S1 and S2†) show that both $Bi_8CsO_8SeCl_7$ and $Bi_8CsO_8SeBr_7$ have the same structures as the reported material $Pb_{0.6}Bi_{3.4}Cs_{0.6}O_4Cl_4$.[25] No impurities were observed in either sample. Rietveld refinements of both materials were performed using TOPAS academic V5 and the refined parameters are given in Tables S1–3.†

$Bi_8CsO_8SeCl_7$ has a van der Waals layered structure consisting of two $[Bi_2O_2]^{2+}$ fluorite layers that are bridged by a cubic $[Cs_{0.5}Cl_2]^{1.5-}$ layer, and are each capped by terminal $[Cl]^-$ layer (Fig. 1c). The Cs^+ in the $[Cs_{0.5}Cl_2]^{1.5-}$ layer occupies the centre of a cubic arrangement of Cl^- ions, similar to that of CsCl but with a half-occupied Cs^+ site. The selenide anions preferentially occupy the terminal $[Cl]^-$ sites over the sites adjacent to Cs^+, as the Cl^- content refines to 1.000(16) in the $[Cs_{0.5}Cl_2]^{1.5-}$ layers, and the anions are fully ordered on this site for $Bi_8CsO_8SeCl_7$, the occupancy of the Cl^- was fixed to 1.0 for the remainder of the refinement. This reflects the stronger bond and more ionic character of Cs–Cl compared to Bi–Se.[28] In contrast, there is slight anion mixing on this site in $Bi_8CsO_8SeBr_7$ as the Br^- occupancy refines to 0.980(6), which is likely due to the more similar ionic radii and electronegativities of the Se^{2-} and Br^-.

The structure of $Bi_8CsO_8SeCl_7$ can also be thought of as Cs^+ occupying alternate van der Waals (vdW) layers of BiOCl which are then stabilized by substitutions of Cl^- for Se^{2-} to balance the charge. The presence of Cs^+ alters the layer stacking of BiOCl. Rather than the layers being staggered, they are offset by half a unit cell along the *ab*-axes to form the cubic environment that the Cs^+ can occupy. However, we note that the Cs^+ site occupancy cannot be varied by adjusting the Cl^- : Se^{2-} ratio, *i.e.* $Bi_8Cs_xO_8Se_xCl_{8-x}$, due to the formation of impurity peaks in the PXRD pattern when $x \neq 1$ (Fig. S3†). Due to the structural and compositional similarities of $Bi_8CsO_8SeCl_7$ to BiOCl, the properties of the two are compared and contrasted throughout the remainder of this paper.

The compositions of the $Bi_8CsO_8SeX_7$ samples discussed above were confirmed by TEM-EDX. The measured compositions of each material were determined to be $Bi_{8.0(3)}Cs_{0.7(3)}Se_{0.96(6)}Cl_{6.9(5)}$ and $Bi_{8.0(2)}Cs_{0.9(3)}Se_{0.97(4)}Br_{7.6(4)}$, respectively. Oxygen was excluded due to the low accuracy of EDX for measurement of light elements. The measured Bi–Cs–Se–X quaternary plots are given in Fig. S4† and, for both samples, the measured elemental ratios are in good agreement with the refined occupancies from neutron diffraction data and show tight clustering around their nominal compositions.

Homologous analogues of $Pb_{0.6}Bi_{3.4}Cs_{0.6}O_4Cl_4$ (the compound that shares its structure with $Bi_8CsO_8SeX_7$) have been reported, for example, $Pb_{1.5}Bi_{2.5}Cs_{0.5}O_4Cl_3$ and $Pb_{0.6}Bi_{1.4}Cs_{0.6}O_2Cl_2$.[25] However, the respective selenide-containing series, $Bi_8CsO_8Se_3Cl_3$ and $Bi_4CsO_4SeCl_3$, could not be made *via* subsolidus routes. The conditions tried are given in the ESI,† and resulting XRD analyses are shown in Fig. S5.†

Both $Bi_8CsO_8SeCl_7$ and $Bi_8CsO_8SeBr_7$ are air-stable, and stable up to 700 K under flowing N_2 as measured by TGA (Fig. S6†). Above 700 K the material volatilises resulting in a small amount of a poorly crystalline powder. Both materials are insoluble in water and their structures are retained after sonication in water for 24 h, although slight increases in the *c*-axes of both materials are observed (Table S4†). This increase likely results from the intercalation of water into the van der Waals gaps.

3.2. Thermal properties

Considering the low thermal conductivities of BiOCl, Bi_2O_2Se and $Bi_4O_4SeCl_2$, the thermal properties of $Bi_8CsO_8SeX_7$ (X = Cl

Open Access Article. Published on 30 June 2023. Downloaded on 12/7/2025 10:16:05 AM.
This article is licensed under a Creative Commons Attribution 3.0 Unported Licence.

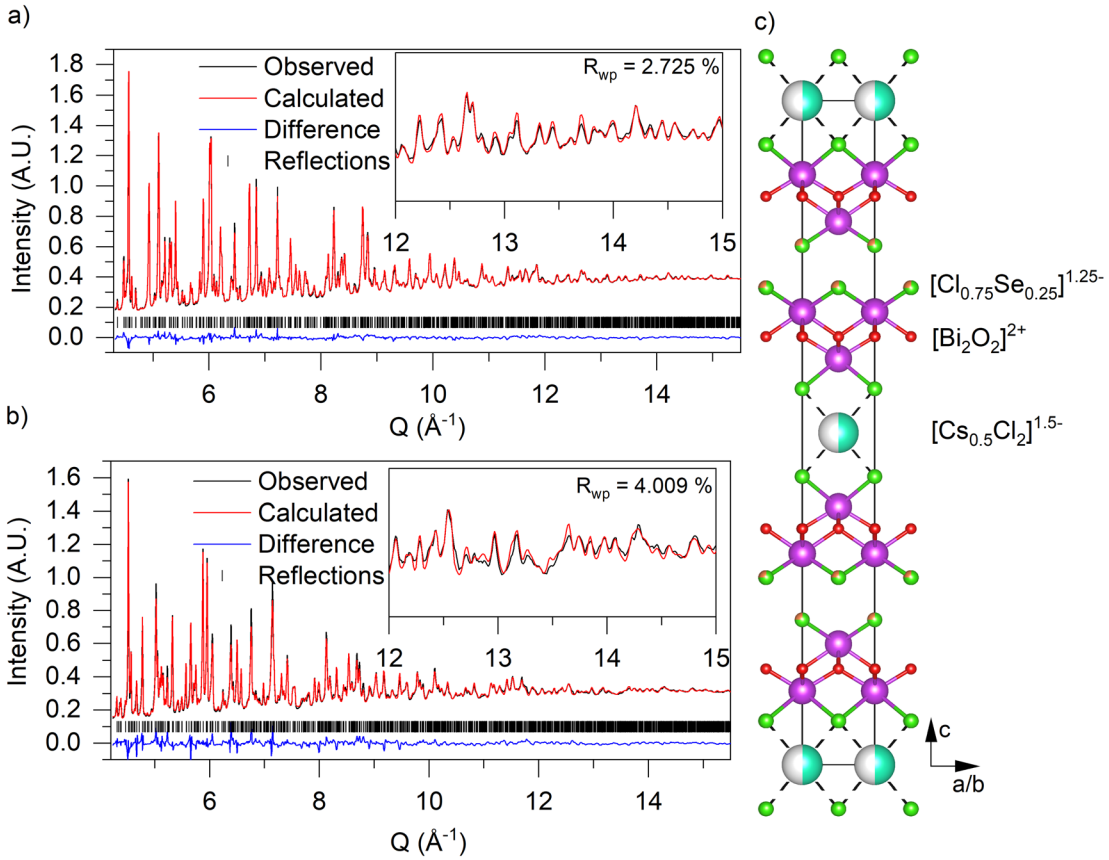

Fig. 1 Rietveld refinement against neutron diffraction data for (a) $Bi_8CsO_8SeCl_7$ and (b) $Bi_8CsO_8SeBr_7$ from NOMAD Bank 5. The insets show the fits of the data at high Q (12–15 Å^{-1}) the black, red, and blue curves represent the observed, calculated, and difference patterns respectively, while the black tick marks show the allowed *hkl* reflections. The structure of $Bi_8CsO_8SeCl_7$ is displayed in (c) where purple, blue, red, orange and green spheres represent Bi^{3+}, Cs^+, O^{2-}, Se^{2-}, and Cl^- respectively.

and Br) were measured, and are shown in Fig. 2a–f. Measurements were performed on dense pellets with significant texturing, with the 00*l* planes being parallel to the pellet face (Fig. S7†). This texturing of the prepared pellets enables extraction of the thermal conductivities along the *c*-axis and within the *ab*-plane by measuring parallel (∥) and perpendicular (⊥) to the pressing direction, respectively. TEM-EDX measurements where made on ground pellets after pressing to confirm that the spark plasma sintering did not result in the volatilisation of any part of the products (Table S5†).

The thermal conductivities of both the $Bi_8CsO_8SeCl_7$ and $Bi_8CsO_8SeBr_7$ pellets exhibit a glass-like temperature dependence that plateaus at 0.27(2) and 0.22(2) W m^{-1} K^{-1}, respectively, when measured parallel to the pressing direction. This linear trend continues up to 600 K when measured by laser flash analysis (Fig. S8†).

The minimum thermal conductivities of both materials were then calculated using the average phonon velocities, which were in turn calculated using the Debye temperatures obtained by fitting the heat capacity data (Fig. 2c–f). This gives a κ_{min} of 0.62 W m^{-1} K^{-1} for $Bi_8CsO_8SeCl_7$, and 0.54 W m^{-1} K^{-1} for $Bi_8CsO_8SeBr_7$ at 300 K. This is particularly unusual as the theoretical minimum is larger than the measured thermal conductivity of each material along the *c*-axis (*i.e.* parallel to the pressing direction). This occurs in $Bi_8CsO_8SeX_7$ because, when measured parallel to the pressing direction, there is considerable bond strength contrast between the vdW gaps and $[Bi_2O_2]^{2+}$ layers. This causes a breakdown in the assumptions made in the Debye–Callaway model. Firstly, this implies that there is a reduction in the acoustic phonon velocity relative to the Debye velocity. Secondly, that there is a large difference between the acoustic and optical phonon velocities where the acoustic phonon cut-off frequency (ω_c) is lower than the Debye frequency (ω_D). The violation of these assumptions that are used to calculate κ_{min} were also observed in BiOCl when measured along the *c*-axis.[14]

The thermal transport properties of both $Bi_8CsO_8SeCl_7$ and $Bi_8CsO_8SeBr_7$ show significant anisotropy, and the thermal conductivities are larger when measured perpendicular to the pressing direction corresponding to the *ab* plane of the structures (Fig. 2a and b). Both materials retain the glass-like temperature dependence observed in the out-of-plane data with no low-temperature peak. The thermal conductivity of $Bi_8CsO_8SeCl_7$ plateaus at 0.83(7) W m^{-1} K^{-1} at 160 K, whereas $Bi_8CsO_8SeBr_7$ plateaus at 0.54(5) W m^{-1} K^{-1} at the same temperature. The lack of a crystalline peak in the thermal

 This journal is © The Royal Society of Chemistry 2023

Open Access Article. Published on 30 June 2023. Downloaded on 12/7/2025 10:16:05 AM.
This article is licensed under a Creative Commons Attribution 3.0 Unported Licence.

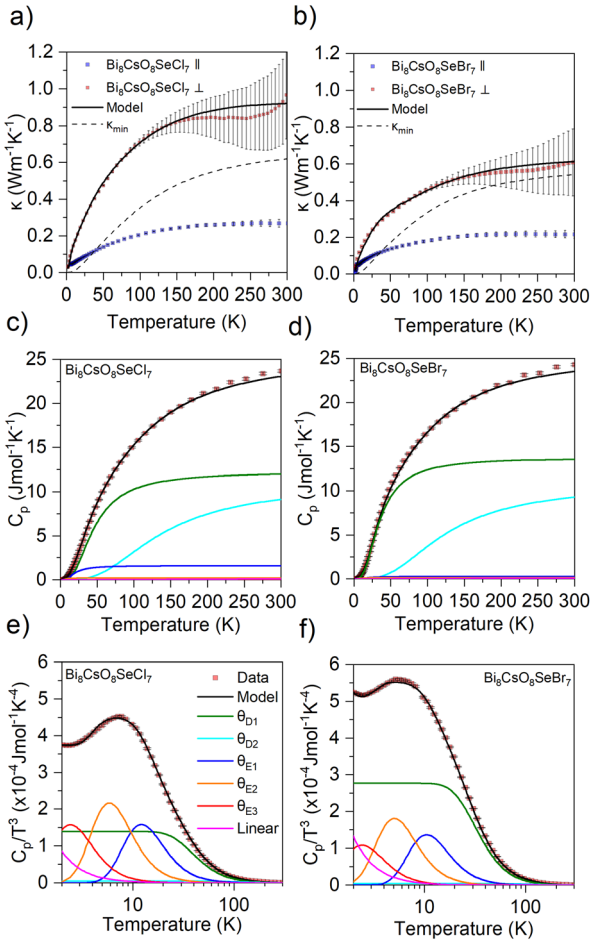

Fig. 2 The thermal conductivities of (a) $Bi_8CsO_8SeCl_7$ and (b) $Bi_8CsO_8SeBr_7$ when measured parallel (||) and perpendicular (⊥) to the pressing direction. The thermal conductivity models, $\kappa_{min,Cl}$, and $\kappa_{min,Br}$ were calculated using the Debye and Einstein temperatures obtained by the fitting of the $C_p(T)$ and $C_p/T^3(T)$ data shown in (c and d) $Bi_8CsO_8SeCl_7$ and (e and f) $Bi_8CsO_8SeBr_7$. The figure legend in (e) represents the fits across all four heat capacity plots, and the vertical markers in each plot indicates the determined uncertainties for each measurement.

conductivities suggests that there is significant phonon scattering in the $Bi_8CsO_8SeX_7$ materials in the low temperature region that supresses the peak in κ typically associated with crystalline materials.[29] This typically arises when phonon mean free paths are reduced by scattering mechanisms to distances that are comparable to interatomic distances. The in-plane thermal conductivity of each material can be modelled as they are above κ_{min}. These models are discussed in detail in Section 3.4 and the ESI.†

The uncertainties in these measurements were determined by the PPMS MultiVu software using a combination of the uncertainty associated with the fits of the thermal relaxation profile, and with the uncertainty associated with the corrections applied for radiative heat loss.[30] For both materials, there is a somewhat large uncertainty in the perpendicular thermal conductivities due to the larger surface-area to volume ratio in four probe measurement geometry which results in greater radiative heat loss corrections. Despite this, the relative uncertainties observed here are consistent with the relative uncertainties in other materials in the literature when measured by the same method, and it is clear that both materials retain the glass-like temperature dependence observed in the parallel measurements with no low-temperature peak.[31]

The heat capacities of $Bi_8CsO_8SeX_7$ were measured and modelled (Fig. 2c–f) using a linear combination of Debye and Einstein terms (see ESI, Table S6†). For both materials, to accurately model the heat capacities at high temperatures (Fig. 2c and d) two Debye temperatures (θ_D) are required: 180(10) K and 555(10) K for $Bi_8CsO_8SeCl_7$, and 360(10) K and 510(10) K for $Bi_8CsO_8SeBr_7$. However, it should be noted that good fits could be obtained with Debye temperatures ±10 K of these values by adjusting the pre-factors of each.

At low temperatures in the $C_p/T^3(T)$ plots (Fig. 2e and f), both materials show an asymmetric peak in the measured data which requires three Einstein temperatures (θ_E) to be modelled. For $Bi_8CsO_8SeCl_7$ these are 59, 29, and 12 K, while for $Bi_8CsO_8SeBr_7$, these are 52, 25, and 12 K. Both materials also require a linear (γ) term of 0.33 and 0.53 mJ mol^{-1} K^{-2}, respectively, to fit the data below 5 K. The γ terms required for $Bi_8CsO_8SeCl_7$ and $Bi_8CsO_8SeBr_7$ are of similar magnitude to the γ term required to model the heat capacity of BiOCl, which is 0.39 mJ mol^{-1} K^{-2}.[14] The heat capacities of $Bi_8CsO_8SeX_7$ cannot be accurately fit with fewer parameters, for example, with only 1 Debye temperature or 2 Einstein temperatures (Fig. S9†).

3.3. Cs^+ rattling in $Bi_8CsO_8SeX_7$

Using $Bi_8CsO_8SeCl_7$ as a representative example, we further investigated the origins behind the low thermal conductivities in these materials as the Cs^+ exhibits some features typical of rattlers. For example, the Cs^+ site is partially occupied, and has a large associated U_{iso} isotropic displacement parameter of 0.0441(17) $Å^2$ when determined by refinements against synchrotron PXRD patterns at 300 K.[32] Further, $Bi_8CsO_8SeCl_7$ has a longer Cs–Cl bond of 3.6205(7) Å compared to 3.574(3) Å in CsCl, which is indicative of weaker bonding interactions, and the body diagonal length of the chloride cage in $Bi_8CsO_8SeCl_7$ is 3.62 Å, which is greater than 3.48 Å diameter of the Cs^+ cation when accounting for the radii of the Cl^-.[33,34] The weaker Cs–Cl bond in $Bi_8CsO_8SeCl_7$ is also supported by calculation of the bond valence sum of Cs^+, as it was determined to have a charge of 0.85+, smaller than the expected 1+ charge.[34,35] Additionally, the very low Einstein temperatures required to fit the plot of $C_p/T^3(T)$ indicates the presence of a low frequency oscillator, possibly an ion with a large mass such as Cs^+.[36]

All of these features are indicative of a loosely bound atom that can disrupt the vibrational modes of its oversized cage.[37–39] To investigate the Cs^+ rattling hypothesis, we refine the U_{iso} of each site between 100 K and 500 K (Fig. 3, Table S7†) from synchrotron VT-PXRD data.

All U_{iso} values increase linearly with temperature, however the $U_{iso}(T)$ of Cs^+ exhibits a much steeper gradient compared to the other elements. This shows a much greater displacement of the Cs^+ ions relative to the others, and is characteristic of

Open Access Article. Published on 30 June 2023. Downloaded on 12/7/2025 10:16:05 AM.
This article is licensed under a Creative Commons Attribution 3.0 Unported Licence.

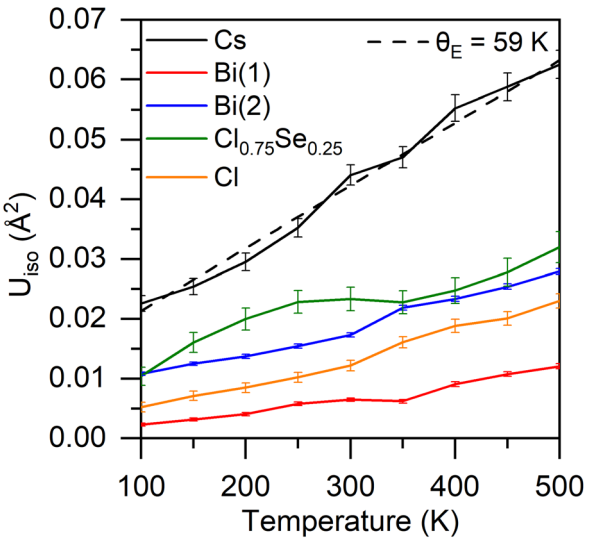

Fig. 3 The refined isotropic displacement parameters (U_{iso}) of each site in $Bi_8CsO_8SeCl_7$ as a function of temperature extracted from synchrotron VT-PXRD data. The dashed line plots the $U_{iso}(T)$ relationship from eqn (1) for a Cs atom with an Einstein temperature of 59 K and a y-intercept of 0.011 Å^2. The error bars represent the standard deviations associated with each refinement.

a rattling site or ion.[40] The Einstein temperature of the Cs^+ can be calculated using the gradient of $U_{iso}(T)$ using eqn (1) and gives a low θ_E of 59(6) K. This is identical to one of the Einstein temperatures (59(2) K) extracted *via* heat capacity measurements, and provides strong evidence for Cs^+ rattling within the structure of $Bi_8CsO_8SeCl_7$, as rattling is a localised vibrational mode.[27] The $U_{iso}(T)$ relationship for a 59 K Einstein oscillator with a mass equal to Cs is overlaid on Fig. 3 as a dashed line. To fit the measured data, a non-zero y-intercept of 0.011 Å^2 must be also included. This non-zero intercept is commonly observed for disordered rattling sites, for example in $Tl_{0.22}Co_4Sb_{12}$ and $Sr_8Ga_{16}Ge_{30}$.[41,42]

We observe that $Cl_{0.75}Se_{0.25}$ site in Fig. 3 has a slightly less linear relationship of $U_{iso}(T)$. This site is adjacent to the van der Waals gap and it is therefore reasonable to expect that there might be a greater uncertainty here compared to the other sites as the weak vdW bonding can result in the layers "slipping" past each other resulting in greater disorder and higher uncertainties in the refinement.

The Debye temperatures associated with the other sites can also be calculated using the gradient of $U_{iso}(T)$ and eqn (2). Using the average gradient associated with the bismuth sites, a calculated Debye temperature of 150(23) K can be obtained which is within error of the lower Debye temperature determined through fitting heat capacity data, 180(10) K (Fig. 2c and e).

While it is likely due to rattling, we rule out other possible origins of the large Cs^+ displacement parameters in $Bi_8CsO_8SeCl_7$. For example, as mobile ions are known to reduce the thermal conductivity of some materials, we investigate the possibility of Cs^+ hopping between neighbouring sites.[17] To achieve this, the total (electronic + ionic) conductivity was assessed by AC impedance spectroscopy, and the electronic contribution of this conductivity was assessed by DC polarisation measurements (Fig. 4).

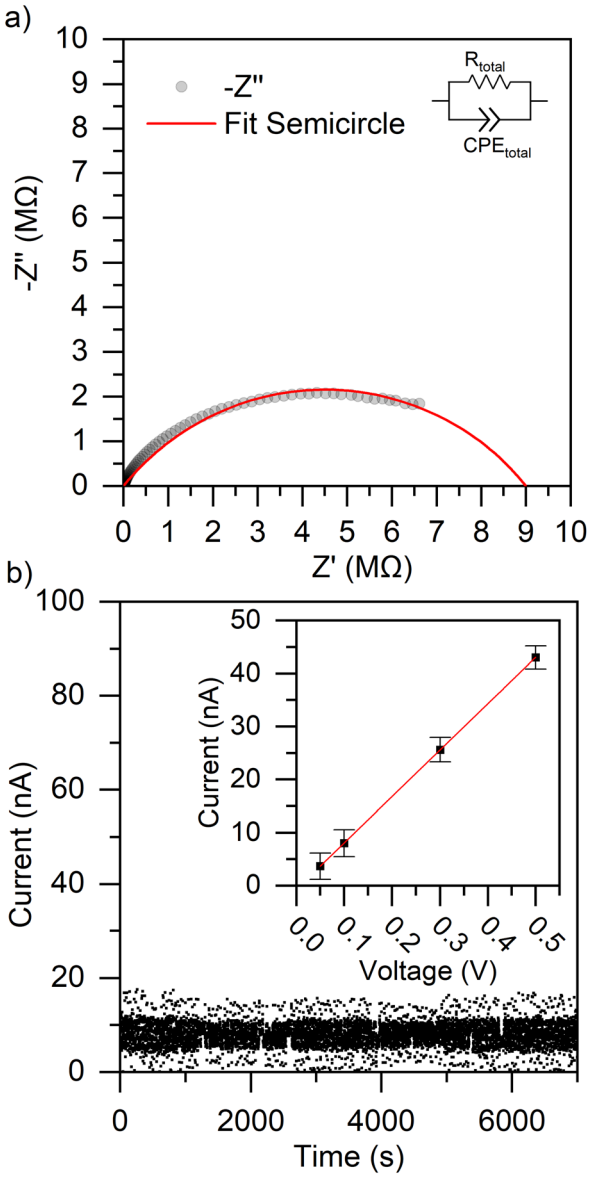

Fig. 4 (a) A Nyquist plot for $Bi_8CsO_8SeCl_7$ with the fit semicircle overlaid. The inset shows the equivalent circuit used to model the data. (b) The DC polarisation data of $Bi_8CsO_8SeCl_7$ at 0.1 V. The inset shows the VI curve obtained from plotting the average current and standard deviations of each measurement at different starting voltages.

The impedance spectrum shows a single semicircle-like relationship between the real and imaginary components with no electrode type feature at low frequencies. The DC polarisation measurements show a single time-independent current when measured at 0.05 V, 0.1 V, 0.3 V and 0.5 V with no tick-like feature at small measurement times (Fig. S10†). The lack of electrode features in AC impedance and tick-like features in DC polarisation indicates that there is no ionic conductivity in $Bi_8CsO_8SeCl_7$ and that the measured conductivity is solely electronic in nature.

 This journal is © The Royal Society of Chemistry 2023

Open Access Article. Published on 30 June 2023. Downloaded on 12/7/2025 10:16:05 AM. This article is licensed under a Creative Commons Attribution 3.0 Unported Licence.

To extract the total (electronic + ionic) conductivity, the impedance spectrum was modelled using ZView2 with a single equivalent circuit containing a resistor and constant phase element (CPE) in parallel.[43] The contribution from the electronic conductivity was determined by plotting the measured current from the DC polarisation measurements against the different starting voltages. The conductivities from DC polarisation and AC impedance where determined to be $1.08(2) \times 10^{-6}$ and $1.4(1) \times 10^{-6}$ S cm^{-1} respectively, agreeing with each other and indicating a negligible ionic contribution.

Finally, we rule out the possibility of the large U_{iso} being as a result of split Cs^+ sites as the observed Fourier maps show no evidence of the Cs^+ nuclear nor electron densities being elongated along any crystallographic axis (Fig. S11†).[42,44] Further, additional Rietveld refinements of the structure with split Cs^+ sites always gave negative and unphysical U_{iso} values for Cs^+.

Following confirmation that the large U_{iso} parameters are a result of Cs^+ rattling, we return to the thermal conductivity models discussed earlier. Indeed, for $Bi_8CsO_8SeCl_7$, in order to obtain any model of the thermal conductivity with a reasonable fit of the data, a 59 K harmonic oscillator must be included in the phonon-lifetime function (see ESI† for details). This 59 K term was extracted from the $C_p/T^3(T)$ plots in Fig. 2c and e, and is supported by the $U_{iso}(T)$ relationship observed for Cs^+ in Fig. 3. In the model, this corresponds to phonons with reduced lifetimes in a frequency range surrounding ω_{59K}, the vibrational frequency of the Cs^+ atom, hence a reduction in the thermal conductivity. This is similarly true for $Bi_8CsO_8SeBr_7$, as a 52 K harmonic oscillator must be included in the phonon-lifetime function in order to adequately fit the thermal conductivity. This temperature was also extracted from the measured heat capacity data (Fig. 2d).

3.4. Structure–property relationships in $Bi_8CsO_8SeX_7$

In the Debye–Callaway model, the thermal conductivity of a material is mainly dependant on 3 things: (1) the acoustic phonon velocity, (2) the optical phonon velocity, and (3) the degree of phonon scattering in the material. $Bi_8CsO_8SeX_7$ combines different structural motifs to effectively minimise the thermal conductivity. The bond strength contrast between the vdW gaps and the $[Bi_2O_2]^{2+}$ layers in the *c*-direction reduces the optical and acoustic phonon velocities, hence why κ is lower than κ_{min} in that direction.[14] The $[Bi_2O_2]^{2+}$ layers have large anharmonicity originating from the Bi^{3+} lone pairs leading to increased phonon scattering and lower κ.[45] The rattling Cs^+ cations result in the resonant scattering of phonons, and finally, the Cs^+ vacancies contribute to point defect phonon scattering.

The Cs^+ vacancies play a significant role in the low thermal conductivity of the material. In the thermal conductivity model for $Bi_8CsO_8SeCl_7$, the point defect scattering pre-factor (A) is calculated to be $9.1(3) \times 10^{-41}$ s^3, which is an order of magnitude larger than if the Cs^+ site is assumed to be fully occupied at $0.62(5) \times 10^{-41}$ s^3. This difference would have a large effect on the thermal conductivity model as, if the Cs^+ sites were fully occupied, κ would reach 1.50 W m^{-1} K^{-1} at room temperature assuming all of the other scattering pre-factors are unaffected. Whereas, in the model of the measured data, κ reaches 0.92 W m^{-1} K^{-1} at room temperature. It is the large contribution from the point defect scattering and resonant scattering processes which dominate at lower temperatures and result in the glass-like thermal conductivity.

There is in fact a smaller mass contrast between disordered anions in $Bi_8CsO_8SeBr_7$ compared to $Bi_8CsO_8SeCl_7$, however this has negligible effect on the point defect contribution towards the phonon lifetime as it is dominated by the contributions from the Cs^+/vacancy point defects, and from the slower phonon velocities in the bromide.

The lower thermal conductivity in $Bi_8CsO_8SeX_7$ along the *c*-axis compared to that along the *ab*-plane is consistent with the interpretation that the bond strength contrast primarily reduces the thermal conductivity along *c* by reducing the phonon velocities, whereas the scattering of phonons due to Cs^+ rattling affects phonon transport in both the in-plane and *c*-directions.

Along the *c*-axis, BiOCl has a lower thermal conductivity (0.15(5) W m^{-1} K^{-1}) than $Bi_8CsO_8SeCl_7$ (0.27(2) W m^{-1} K^{-1}) at room temperature, as filling alternate vdW gaps in BiOCl with Cs^+ reduces the amount of bond strength contrast in $Bi_8CsO_8SeCl_7$.[14] In comparison, along the *ab*-plane, the room temperature thermal conductivity of $Bi_8CsO_8SeCl_7$ (0.9(2) W m^{-1} K^{-1}) is lower than that of BiOCl (1.2(1) W m^{-1} K^{-1}).[14] This occurs because, as there are no vdW gaps along the *ab*-plane in $Bi_8CsO_8SeCl_7$, phonons are predominantly scattered by the Cs^+ rattling which is not present in BiOCl. This highlights the importance of understanding and controlling anisotropy through the combination of unique structural motifs in order to control phonon behaviour within such materials. The thermal conductivity observed in $Bi_8CsO_8SeX_7$ is also shown in comparison to other low thermal conductivity materials with similar chemistries in Fig. S12.†[10,11,14]

The main feature that reduces the thermal conductivity in $Bi_8CsO_8SeX_7$ is the bond strength contrast between the van der Waals gaps and the $[Bi_2O_2]^{2+}$ layers. This feature affects phonon transport primarily along the *c*-direction, leading to very anisotropic phonon propagation. As a result, the thermal conductivity along the *c*-axis is greatly supressed in both materials (to similar values) as the degree of bond strength contrast is almost identical.

Comparatively, within the *ab*-plane, the bond strength contrast in $Bi_8CsO_8SeX_7$ has very little effect on the measured thermal conductivity. This results in greater anisotropy in the chloride compared to the bromide as the higher mass of the Br^- anion has a more appreciable effect on the thermal conductivity within the *ab*-plane. The higher mass of the bromide also results in smaller Debye temperatures and therefore slower phonon velocities (Table S8†).[46] The larger mass of Br^- also has the effect of increasing the Umklapp scattering pre-factor in the phonon lifetime function for $Bi_8CsO_8SeBr_7$, as it is proportional to the average atomic mass.[47] This has the effect of reducing the thermal conductivity of $Bi_8CsO_8SeBr_7$ to close to that of κ_{min} at high temperatures.

3.5. Band gaps

$Bi_8CsO_8SeX_7$ has a combination of bond strength anisotropy from the vdW gaps, and low frequency Cs^+ rattling. Both of

Open Access Article. Published on 30 June 2023. Downloaded on 12/7/2025 10:16:05 AM.
This article is licensed under a Creative Commons Attribution 3.0 Unported Licence.

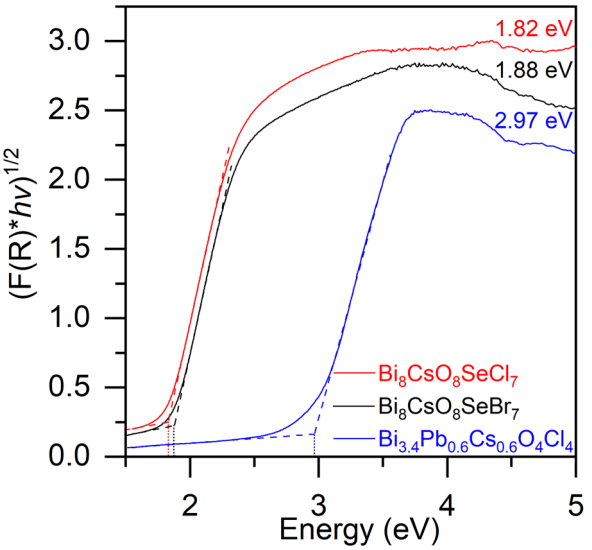

Fig. 5 Tauc plots of $Bi_8CsO_8SeX_7$ (X = Cl, Br), and of $Bi_{3.4}Pb_{0.6}Cs_{0.6}O_4Cl_4$.

which contribute to reduce the thermal conductivity of the material along different crystallographic directions. As part of an investigation of possible applications for $Bi_8CsO_8SeX_7$, we measure their optical band gaps (Fig. 5). For comparison, we also synthesised $Bi_{3.4}Pb_{0.6}Cs_{0.6}O_4Cl_4$ (Fig. S13†) to investigate the extent to which Bi^{3+}-for-Pb^{2+} and Se^{2-}-for-Cl^- substitutions can be used to control and reduce the band gap.

$Bi_8CsO_8SeCl_7$ and $Bi_8CsO_8SeBr_7$ have indirect bandgaps of 1.82(3) eV and 1.88(3) eV respectively, which are too wide for thermoelectric applications. These large band gaps result in the high electrical resistivity that was observed in the DC polarisation measurement of $Bi_8CsO_8SeCl_7$. However, the band gaps of $Bi_8CsO_8SeX_7$ (X = Cl, Br) are significantly reduced compared to $Bi_{3.4}Pb_{0.6}Cs_{0.6}O_4Cl_4$ (2.97(3) eV) due to the substitution of Se^{2-} for Cl^-. Future investigations into a homologous series containing $Bi_8CsO_8SeX_7$ with differing $X^-:Se^{2-}$ ratios may allow for further optimisation of the band structure and carriers for thermoelectric applications.[48,49] The layered nature of the structure also likely make the materials more amenable to combination with other structural motifs to further tune the electronic transport properties, such as the introduction of [BiCuSeO] layers, similar to $Bi_6Cu_2Se_4O_6$.[50] Additional routes to doping the materials to increase electronic conductivity and tune the Seebeck coefficient could involve substitution of the Bi^{3+} or any of the available anion sites.[51]

For the same reason, the $Bi_8CsO_8SeX_7$ materials also have narrower optical band gaps compared to the structurally and compositionally similar BiOCl. As a result, they may exhibit potential as photocatalysts where BiOCl is currently used. This could be of particular interest in hydrogen evolution reactions, for example, as $Bi_8CsO_8SeX_7$ has a similar layered structure and composition to BiOCl, but also a band gap that allows for absorption of visible light, rather than solely in the UV region.[21] Similar layered materials have also been investigated for their high dielectric constants and dangling-bond-free surfaces for use in nanoelectronics.[52,53]

4. Conclusion

To conclude, we present two mixed-anion materials, $Bi_8CsO_8SeX_7$ (X = Cl and Br) that were synthesised based on Bi^{3+}-for-Pb^{2+} and Se^{2-}-for-Cl^- substitutions in $Bi_{3.4}Pb_{0.6}Cs_{0.6}O_4Cl_4$. These materials contain a combination of heavy atoms, sharp bond strength contrast, Cs^+ vacancies, and low frequency Cs^+ rattling, all of which contribute to reduce the thermal conductivity of the materials to a minimum of 0.22(2) $W\,m^{-1}\,K^{-1}$ along the *c*-axis at room temperature. The thermal conductivities of $Bi_8CsO_8SeX_7$ are highly anisotropic as bond strength contrast is the dominant feature to inhibit phonons along the *c*-axes, while low frequency Cs^+ rattling dominates along the *ab*-planes. This highlights how different structural motifs can be used to design and identify new materials with low thermal conductivities, as well as the importance of understanding and controlling anisotropy.

Author contributions

J. A. Newnham, conceptualisation, investigation, formal analysis, visualisation, writing – original draft, writing – review & editing; Q. D. Gibson, formal analysis, writing – original draft, writing – review & editing; T. W. Surta, formal analysis, writing – review & editing; A. Morscher, formal analysis, writing – review & editing; T. D. Manning, supervision, writing – review & editing; L. M. Daniels, supervision, writing – review & editing; J. B. Claridge, supervision, funding acquisition; M. J. Rosseinsky, writing – review & editing, supervision, funding acquisition, project administration.

Conflicts of interest

There are no conflicts to declare.

Acknowledgements

The authors thank the Engineering and Physical Science Research Council (EPSRC) for funding under EP/N004884/1 and EP/V026887/1. This research made use of the NOMAD instrument at the Spallation Neutron Source, a DOE Office of Science User Facility operated by the Oak Ridge National Laboratory. We thank Diamond Light Source for access to beamline I11 (proposal CY23666). We acknowledge the ICSF Faraday Challenge project "All-Solid State Lithium Anode Battery 2" [grant number FIRG026] for funding AM.

References

1 M. Hamid Elsheikh, D. A. Shnawah, M. F. M. Sabri, S. B. M. Said, M. Haji Hassan, M. B. Ali Bashir and M. Mohamad, *Renewable Sustainable Energy Rev.*, 2014, **30**, 337–355.
2 D. R. Clarke and S. R. Phillpot, *Mater. Today*, 2005, **8**, 22–29.
3 B. Hu, X. L. Shi, J. Zou and Z. G. Chen, *Chem. Eng. J.*, 2022, **437**, 135268.

 This journal is © The Royal Society of Chemistry 2023

Open Access Article. Published on 30 June 2023. Downloaded on 12/7/2025 10:16:05 AM. This article is licensed under a Creative Commons Attribution 3.0 Unported Licence.

4 C. Chiritescu, D. G. Cahill, N. Nguyen, D. Johnson, A. Bodapati, P. Keblinski and P. Zschack, *Science*, 2007, **315**, 351–353.
5 M. T. Agne, R. Hanus and G. J. Snyder, *Energy Environ. Sci.*, 2018, **11**, 609–616.
6 S. Mukhopadhyay, D. S. Parker, B. C. Sales, A. A. Puretzky, M. A. McGuire and L. Lindsay, *Science*, 2018, **360**, 1455–1458.
7 D. G. Cahill, S. K. Watson and R. O. Pohl, *Phys. Rev. B: Condens. Matter Mater. Phys.*, 1992, **46**, 6131.
8 W. Kim, *J. Mater. Chem. C*, 2015, **3**, 10336–10348.
9 K. Biswas, J. He, I. D. Blum, C.-I. Wu, T. P. Hogan, D. N. Seidman, V. P. Dravid and M. G. Kanatzidis, *Nature*, 2012, **489**, 414–418.
10 X.-L. Shi, W.-D. Liu, M. Li, Q. Sun, S.-D. Xu, D. Du, J. Zou, Z.-G. Chen, X.-L. Shi, Z.-G. Chen, W.-D. Liu, M. Li, S.-D. Xu, D. Du, J. Zou and Q. Sun, *Adv. Energy Mater.*, 2022, **12**, 2200670.
11 M. Dutta, S. Matteppanavar, M. V. D. Prasad, J. Pandey, A. Warankar, P. Mandal, A. Soni, U. V. Waghmare and K. Biswas, *J. Am. Chem. Soc.*, 2019, **141**, 20293–20299.
12 E. S. Toberer, A. Zevalkink and G. J. Snyder, *J. Mater. Chem.*, 2011, **21**, 15843–15852.
13 Q. D. Gibson, T. D. Manning, M. Zanella, T. Zhao, P. A. E. Murgatroyd, C. M. Robertson, L. A. H. Jones, F. McBride, R. Raval, F. Cora, B. Slater, J. B. Claridge, V. R. Dhanak, M. S. Dyer, J. Alaria and M. J. Rosseinsky, *J. Am. Chem. Soc.*, 2020, **142**, 847–856.
14 Q. D. Gibson, T. Zhao, L. M. Daniels, H. C. Walker, R. Daou, S. Hébert, M. Zanella, M. S. Dyer, J. B. Claridge, B. Slater, M. W. Gaultois, F. Corà, J. Alaria and M. J. Rosseinsky, *Science*, 2021, **373**, 1017–1022.
15 P. Acharyya, T. Ghosh, K. Pal, K. S. Rana, M. Dutta, D. Swain, M. Etter, A. Soni, U. V. Waghmare and K. Biswas, *Nat. Commun.*, 2022, **13**, 5053.
16 M. K. Jana and K. Biswas, *ACS Energy Lett.*, 2018, **3**, 1315–1324.
17 H. Liu, X. Shi, F. Xu, L. Zhang, W. Zhang, L. Chen, Q. Li, C. Uher, T. Day and G. J. Snyder, *Nat. Mater.*, 2012, **11**, 422–425.
18 M. D. Nielsen, V. Ozolins and J. P. Heremans, *Energy Environ. Sci.*, 2013, **6**, 570–578.
19 S. K. Saha, *Phys. Rev. B: Condens. Matter Mater. Phys.*, 2015, **92**, 041202.
20 Z.-H. Zheng, X.-L. Shi, D.-W. Ao, W.-D. Liu, M. Li, L.-Z. Kou, Y.-X. Chen, F. Li, M. Wei, G.-X. Liang, P. Fan, G. Q. Lu and Z.-G. Chen, *Nat. Sustain.*, 2022, **6**, 180–191.
21 W. Li, S. ao He, Z. ying Su, W. Xu and X. chuan Wang, *Appl. Surf. Sci.*, 2019, **470**, 707–715.
22 P. Ruleova, C. Drasar, P. Lostak, C. P. Li, S. Ballikaya and C. Uher, *Mater. Chem. Phys.*, 2010, **119**, 299–302.
23 N. Imanaka, K. Okamoto, G.-Y. Adachi, N. Imanaka, K. Okamoto and G.-Y. Adachi, *Angew. Chem., Int. Ed.*, 2002, **41**, 3890–3892.
24 H. Kageyama, K. Hayashi, K. Maeda, J. P. Attfield, Z. Hiroi, J. M. Rondinelli and K. R. Poeppelmeier, *Nat. Commun.*, 2018, **9**, 772.
25 D. O. Charkin, P. S. Berdonosov, A. M. Moisejev, R. R. Shagiakhmetov, V. A. Dolgikh and P. Lightfoot, *J. Solid State Chem.*, 1999, **147**, 527–535.
26 A. A. Coelho, *J. Appl. Crystallogr.*, 2000, **33**, 899–908.
27 B. C. Sales, D. G. Mandrus and B. C. Chakoumakos, *Semicond. Semimetals*, 2001, **70**, 1–36.
28 T. P. Debies and J. W. Rabalais, *Chem. Phys.*, 1977, **20**, 277–283.
29 G. S. Nolas, J. Sharp and H. J. Goldsmid, in *Thermoelectrics*, Springer, Berlin, Heidelberg, 2001, pp. 177–207.
30 *Physical Property Measurement System Thermal Transport Option User's Manual*, Quantum Design.
31 A. Das, K. Pal, P. Acharyya, S. Das, K. Maji and K. Biswas, *J. Am. Chem. Soc.*, 2023, **145**, 1349–1358.
32 B. C. Sales, B. C. Chakoumakos, D. Mandrus and J. W. Sharp, *J. Solid State Chem.*, 1999, **146**, 528–532.
33 W. Qiu, L. Xi, P. Wei, X. Ke, J. Yang and W. Zhang, *Proc. Natl. Acad. Sci. U.S.A.*, 2014, **111**, 15031–15035.
34 M. Sist, K. Frederik FaerchF ischer, H. Kasai, B. Brummerstedt Iversen, D. Sist, K. F. F Fischer, H. Kasai, B. B. Iversen and D. Kasai, *Angew. Chem., Int. Ed.*, 2017, **56**, 3625–3629.
35 N. E. Brese and M. O'Keeffe, *Acta Crystallogr., Sect. B: Struct. Sci.*, 1991, **47**, 192–197.
36 R. P. Hermann, R. Jin, W. Schweika, F. Grandjean, D. Mandrus, B. C. Sales and G. J. Long, *Phys. Rev. Lett.*, 2003, **90**, 135505.
37 D. J. Voneshen, K. Refson, E. Borissenko, M. Krisch, A. Bosak, A. Piovano, E. Cemal, M. Enderle, M. J. Gutmann, M. Hoesch, M. Roger, L. Gannon, A. T. Boothroyd, S. Uthayakumar, D. G. Porter and J. P. Goff, *Nat. Mater.*, 2013, **12**(11), 1028–1032.
38 G. S. Nolas, J. L. Cohn, G. A. Slack and S. B. Schujman, *Appl. Phys. Lett.*, 1998, **73**, 178.
39 G. Nolas and J. Cohn, *Phys. Rev. B: Condens. Matter Mater. Phys.*, 1998, **58**, 164.
40 P. Vaqueiro, R. A. R. Al Orabi, S. D. N. Luu, G. Guélou, A. V. Powell, R. I. Smith, J. P. Song, D. Wee and M. Fornari, *Phys. Chem. Chem. Phys.*, 2015, **17**, 31735–31740.
41 B. Sales, B. Chakoumakos and D. Mandrus, *Phys. Rev. B: Condens. Matter Mater. Phys.*, 2000, **61**, 2475.
42 B. C. Chakoumakos, B. C. Sales, D. G. Mandrus and G. S. Nolas, *J. Alloys Compd.*, 2000, **296**, 80–86.
43 D. Johnson, *ZView*, Scribner Associates Inc., Version 3.5, 2007.
44 M. Ladd and R. Palmer, *Structure Determination by X-ray Crystallography*, Springer, New York, 5th edn, 2013.
45 Y.-L. Pei, J. He, J.-F. Li, F. Li, Q. Liu, W. Pan, C. Barreteau, D. Berardan, N. Dragoe and L.-D. Zhao, *NPG Asia Mater.*, 2013, **5**, e47–e55.
46 F. J. DiSalvo, *Science*, 1999, **285**, 703–706.
47 J. Yang, in *Thermal Conductivity*, ed. T. M. Tritt, Springer, Boston, MA, 2004, pp. 1–20.
48 Q. D. Gibson, M. S. Dyer, C. Robertson, C. Delacotte, T. D. Manning, M. J. Pitcher, L. M. Daniels, M. Zanella, J. Alaria, J. B. Claridge and M. J. Rosseinsky, *Inorg. Chem.*, 2018, **57**, 12489–12500.

49 Q. D. Gibson, J. A. Newnham, M. S. Dyer, C. M. Robertson, M. Zanella, T. W. Surta, L. M. Daniels, J. Alaria, J. B. Claridge and M. J. Rosseinsky, *J. Solid State Chem.*, 2022, **312**, 123246.
50 X. Zhang, Y. Qiu, D. Ren and L. D. Zhao, *Ann. Phys.*, 2020, **532**, 1900340.
51 J. A. Newnham, T. Zhao, Q. D. Gibson, T. D. Manning, M. Zanella, E. Mariani, L. M. Daniels, J. Alaria, J. B. Claridge, F. Corà and M. J. Rosseinsky, *ACS Org. Inorg. Au*, 2022, **2**, 405–414.
52 C. Zhang, T. Tu, J. Wang, Y. Zhu, C. Tan, L. Chen, M. Wu, R. Zhu, Y. Liu, H. Fu, J. Yu, Y. Zhang, X. Cong, X. Zhou, J. Zhao, T. Li, Z. Liao, X. Wu, K. Lai, B. Yan, P. Gao, Q. Huang, H. Xu, H. Hu, H. Liu, J. Yin and H. Peng, *Nat. Mater.*, 2023, **2023**, 1–6.
53 J. N. Coleman, Y. Nalawade, J. Pepper, A. Harvey, A. Griffin, D. Caffrey and A. G. Kelly, *ACS Appl. Electron. Mater.*, 2020, **2**, 3233–3241.

Open Access Article. Published on 30 June 2023. Downloaded on 12/7/2025 10:16:05 AM.
This article is licensed under a Creative Commons Attribution 3.0 Unported Licence.

This journal is © The Royal Society of Chemistry 2023